Measurement 188 (2022) 110373

Contents lists available at ScienceDirect

Measurement

journal homepage: www.elsevier.com/locate/measurement

Focused ion beam-based microfabrication of boron-doped diamond single-crystal tip cantilevers for electrical and mechanical scanning probe microscopy

Ewelina Gacka [a,*], Piotr Kunicki [a], Andrzej Sikora [a], Robert Bogdanowicz [b], Mateusz Ficek [b], Teodor Gotszalk [a], Ivo W. Rangelow [c], Krzysztof Kwoka [a]

[a] Department of Nanometrology, Faculty of Electronics, Photonics and Microsystems, Wrocław University of Science and Technology, 11/17 Janiszewskiego Street, 50-372 Wrocław, Poland
[b] Department of Metrology and Optoelectronics, Faculty of Electronics, Telecommunications and Informatics, Gdańsk University of Technology, 11/12 Gabriela Narutowicza Street, 80-233 Gdańsk, Poland
[c] Nanoskalige Systeme, Ilmenau University of Technology, Gustav-Kirchhoff-Str. 1, D-98684 Ilmenau, Germany

ARTICLE INFO

Keywords:
Single-crystal boron-doped diamond microparticle
Focused ion beam
Scanning electron microscope, Microcantilever
Diamond tip
Scanning probe microscope

ABSTRACT

In this paper, the fabrication process and electromechanical properties of novel atomic force microscopy probes utilising single-crystal boron-doped diamond are presented. The developed probes integrate scanning tips made of chemical vapour deposition-grown, freestanding diamond foil. The fabrication procedure was performed using nanomanipulation techniques combined with scanning electron microscopy and focused ion beam technologies. The mechanical properties of the cantilever were monitored by the measurement of thermally induced vibration of the cantilever after every fabrication step, allowing the mass changes in range of ng to be estimated. The endurance of the developed probes was tested during hundreds of topography measurements, which corresponds to a scanning length equal to 13.6 m, performed on a test sample in contact and lateral force microscopy modes. Analysis of the roughness parameters confirmed the extremely high wear resistance of the fabricated probes. The linear current voltage response on a highly-oriented pyrolytic graphite sample was recorded.

1. Introduction

In recent years, many efforts have been made to test various materials and structures of so-called atomic force microscopy (AFM) cantilevers. The general aim of these investigations has been to develop devices with limited stiffness and a high resonance frequency integrating probes with a high aspect ratio and resistant against wear. In this context, diamond was a promising material characterised by high mechanical durability, hardness, Young's modulus and chemical stability [1]. Moreover, considering the growing need for the reliable nanoscale diagnostic of electrical surface properties, diamond-based tools seem to be very attractive especially for AFM-based nanometrology.

In conductive atomic force microscopy (C-AFM), a biased conductive tip collects a current flowing from the surface. In this way, it is possible to image the local electrical surface properties [2]. However, the local resolution depends strongly on the tip properties, which can vary during surface scanning. It is noteworthy that cantilevers with diamond tips are useful for nanolithography, and on the contrary to the commercial silicon (Si) beams, they are characterised by the increased stability of the field emission (FE) and reduced wear caused by the current flow [3]. Moreover, diamond tips do not evaporate under the current load, in contrast to the commercial tips coated with metal layers [4].

Diamond intrinsically exhibits low conductivity attributed mainly to C-H defects and hydrogen termination [5]. Doping of diamond with boron makes it possible to control and influence its electrical conductivity with various carrier transport mechanisms [6]. Polycrystalline boron-doped diamond (BDD) reveals unique electronic properties being a p-type semiconductor [7] applied in electronics [8], electrochemistry [9–10] and microelectromechanical systems (MEMS) [11]. Its high conductivity, low dielectric constant and wide energy gap enables the efficient application of BDD to passive electronic (resistors, capacitors, dielectrics, passivation and protecting layers [12]) and electromechanical devices.

BDD particles can be fabricated by various approaches such as ball-

* Corresponding author.
E-mail address: ewelina.gacka@pwr.edu.pl (E. Gacka).

https://doi.org/10.1016/j.measurement.2021.110373
Received 11 May 2021; Received in revised form 19 September 2021; Accepted 20 October 2021
Available online 1 November 2021

assisted milling of high pressure high temperature (HPHT) [13] diamond material or alternatively chemical vapour deposition (CVD) [14], overgrowth of intrinsic diamond [15] and isolated single-crystal synthesis [16] in the CVD process. Several various works have reported CVD diamond applied for nanomechanical devices as tips or cantilevers [17].

Hoffman *et al.* [18] reported a H-terminated diamond-tip for field emission scanning probe lithography generation features with half pitches below 15 nm. The probe revealed enhanced mechanical performance along with FE stability throughout 48 h of testing. Diamond particles deposited by hot filament chemical vapour deposition (HFCVD) on regular systems such as Si tips prepared on a Si (1 1 1) resulted in faceted growth of spherical shapes, which were sharpened to achieve nanometric curvature radii. Fabricated diamond emitters can be capable of sustaining currents up to 450 μA with heat conductivity considerably better than copper. The stable electron emission can be explained by the negative electron affinity of diamond, which allows an injection of electrons from diamond at low electric fields.

The main approach presented in the literature is the overgrowth of a pre-formed Si cantilever or tip by diamond film in the CVD process. These important works show that such devices could be applied for advanced investigations as electrochemical (EC) imaging [19] or conductivity imaging tools [20]. Such a process results in an increase in resonance frequencies and quality factor, while the smallest apex radius of 5 nm was achieved by plasma etching applying self-organised metal nanomasks [19]. A much larger top radius of 50 nm was reported by Eifert *et al.* [20] using focused ion beam (FIB) milling. The reported sputtering yields of diamond reveals values in the range of 0.07–0.09 m^3/nC [21]. Interestingly, the EC properties, thus the electronic band structure, may be significantly improved by FIB treatment, followed by EC cycling, manifesting increased electron transfer by *ca.* four orders of magnitude when compared to a pristine sample [22] and could be strongly affected by the milling orientation [23]. It has been already shown that boron is more efficiently incorporated into (1 1 1) facets than into (1 0 0) causing local electrical heterogeneities [24]. A similar methodology was applied by Olbrich *et al.* [2] achieving a higher aspect ratio of 1:7 at a curvature of 30 nm. Hu *et al.* [23] demonstrated that unique electrical and EC properties were achieved using conducting side-on FIB milling, resulting in a minor influence of the generation of defects or diamond amorphisation.

All-diamond conductive tips were developed and reported by Arstila *et al.* [25] using BDD grown on nickel via HFCVD, and by Oesterschulze *et al.* [26] utilising deposition on nanostructured Si wafers. The former study reported tips with a radius of above 500 nm applicable for scanning spreading resistance measurements, while the latter work manifested curvatures of 50 nm revealing its usefulness for nanomachining in-plane gate GaAs/AlGaAs transistors. The oxygen-etched CVD diamond was utilised as a source of lateral facets (1 0 0) with a pyramidal geometry, which were attached to the standard Si/SiN cantilevers [27]. This results in a stiffness of 0.01 N/m at a force of 10^{-12} N for tips of apex radii in the range of 2–10 nm.

Recently, authors reported on coated cantilevers using boron-doped nanocrystalline diamond (BD-NCD) revealing a work function of 4.65 eV along with a spring constant and resonance frequency of 3.2 N/m and 35.87 kHz, respectively [28].

In this paper, a novel fabrication technology of Si cantilevers integrating BDD tips is presented. The entire process starts with CVD growth and isolation of free-standing single BDD crystals. Nanomanipulation techniques combined with the focused electron beam-induced deposition (FEBID) and focused ion beam-induced deposition (FIBID) procedures were applied to place the BDD crystal on a Si cantilever. FIB milling was used to form a tip shape of proper geometry and symmetry.

The advantage of the proposed approach relies on the mechanical probe structure, which was formed by a single-crystal material increasing its insusceptibility against thermal drift. The high current densities occurring in the vicinity of the tip and therefore the increase of material temperature will not influence the changes in height of the diamond tip compared to commercially used ones. Moreover, the reliability of the mechanical calibration performed for such a probe was enhanced, which influences the accuracy of the load force definition in all contact AFM imaging modes. The fabricated probes were tested utilising measurements of the electrical resistance on a highly-oriented pyrolytic graphite (HOPG). The BDD tip's insusceptibility to mechanical wear was proven by multiple imaging of a SiO_2/Cr test structure and SiO_2/Au topography imaging.

2. Materials and methods

2.1. Growth and isolation of single-crystal boron-doped diamond particle

First, BDD film was grown using a microwave plasma enhanced chemical vapour deposition system (SEKI Technotron AX5400S, Japan) on a 1x1 cm mirror-polish Tantalum foil (Sigma-Aldrich Chemie, 0.025 mm thick, 99.9+% metal basis). The detailed parameters of the BDD film synthesis were already reported elsewhere [29–30]. In this experiment, the growth time was set to 180 min resulting in the formation of a polycrystalline BDD nanosheet with a thickness of approximately 1 μm. Next, the BDD nanosheet was mechanically separated from the Ta substrate and transferred to a vessel with 10 ml of 2-propanol. The vessel was positioned for 20 min in an ultrasound homogeniser equipped with a horn-type TS 106 sonotrode (Bandelin Sonopuls HD 4200, Germany). A continuous operation mode with 50% amplitude was utilised to disintegrate the polycrystalline nanosheet to separate the single-crystal boron-doped diamond (SC-BDD) particles. Ultrasound treatment results in the formation of a wide range of single-crystal diamond particles and clusters with various shapes and sizes. The prepared suspension was dropped on a marked Si wafer and dried under room temperature conditions. The sample was placed in a dual beam scanning electron microscopy with focused ion beam (SEM/FIB) system for imaging and nanomanipulation enabling selection of a specific single-crystal diamond and its transfer on the cantilever.

2.2. Scanning electron microscopy and focused ion beam technology

A dual beam SEM/FIB system (Helios NanoLab 600i) was used in the performed experiments. It integrated an electron beam (e-beam) column operating with a current and an acceleration voltage ranging from 1.3 pA and 22 nA and from 300 V up to 30 kV, respectively. A Ga ion column operating with a current up to 65 nA at an acceleration voltage up to 30 kV was used to form the BDD crystals and prepare the Si cantilever for the tip integration. An easy-lift nanomanipulator was utilised to select and place the BDD crystals on the Si cantilever. Focused electron beam-induced deposition (FEBID) and focused ion beam-induced deposition (FIBID) technology was applied to fix its position and enhance the electrical contact with the spring beam [31]. In this case, a gas injection system (GIS) introduced metalorganic precursor molecules ($MeCpPtMe_3$) from the nozzle into the vicinity of the sample surface. The e-beam enabled the molecule decomposition forming a platinum carbon (Pt(C)) structure around the BDD tip. Energy dispersive spectroscopy (EDS) was applied to monitor the composition and homogeneity of the materials of the manufactured structure.

2.3. Raman spectroscopy

The investigation of the molecular composition of the electrodes was carried out by means of Raman spectroscopy. A Horiba LabRAM ARAMIS Raman confocal microscope (100 × /0.95 objective, 50 μm of confocal aperture) equipped with a 532 nm diode-pumped solid-state laser was used. Spectra were recorded in a range of 200–2000 cm^{-1}.

2.4. Cantilever and process metrology

The fabrication process of the cantilever with the BDD tip was

characterised based on the analysis of the noise of the vibration of the thermomechanical structure. In this case, according to the equipartition theorem, a certain amount of the energy is assigned to each mode of the cantilever vibration at a temperature above 0 K. This energy is described by the equation $E_{ET} = 1/2k_BT$, where k_B is the Boltzmann constant and T is the temperature. Moreover, the energy associated with deflection of the cantilever is equal to $E_P = 1/2k\langle x^2\rangle$ (k is the cantilever stiffness and $\langle x^2\rangle$ is the mean square deflection of the cantilever) [32–33]. Therefore, the cantilever stiffness of the vibrating structure can be determined by the formula: $k = \frac{k_BT}{\langle x^2\rangle}$.

The measurement of the thermomechanical noise was performed with a SIOS Meßtechnik GmbH laser vibrometer [34] working in the Michelson configuration and dedicated software. The output signals were acquired using dedicated analogue-to-digital converter electronics. Investigations were undertaken in order to ensure the necessary repeatability and reliability of the performed thermomechanical studies. The spot of the interferometer laser was always focussed at the same spot of the cantilever back-side. In every experiment, the laser was adjusted to obtain analogous power of the signal reflected from the sample.

The recorded cantilever vibration curves were analysed according to the procedure proposed by Riet *et al.* [35]. In this case, the thermomechanical fundamental resonance peak of the cantilever, according to the model of the simple harmonic oscillator (SHO), can be described by the equation [36–37] (1):

$$S_T(f) = \frac{2k_BTf_0^3}{\pi kQ}\left(\frac{1}{\left(f_0^2 - f^2\right)^2 + \left(\frac{f_0 f}{Q}\right)^2}\right) \tag{1}$$

where: $S_T(f)$ is the power spectrum of the thermomechanical noise, f_0 – resonance frequency, Q – quality factor, and f is the vibration frequency. The cantilever stiffness can be determined by (2):

$$k = \frac{2k_BTf_0^3}{\pi AQ} \tag{2}$$

where: A is the fitting parameter.

Furthermore, for the SHO model, the cantilever resonance frequency is described by the equation $f_1 = \frac{1}{2\pi}\sqrt{k/m}$, where m is the effective structure mass. The FIB milling of the probe leads to the change of the structure mass by Δm and consequently to the change of the resonance frequency. In this case, the resonance frequency f_2 of the structure after the FIB process is $f_2 = \frac{1}{2\pi}\sqrt{\frac{k}{m+\Delta m}}$. Thus, the mass change can be calculated using the formula (3):

$$\Delta m = \frac{k}{4\pi^2}\left(\frac{(f_1 - f_2)(f_1 + f_2)}{(f_1 \cdot f_2)^2}\right) \tag{3}$$

The mass change was calculated for the specific resonance frequencies recorded in the subsequent process steps.

2.5. Atomic force microscope investigations

A DI3000 AFM (Digital Instruments, USA) working in ambient conditions (temperature 297 K, RH 34%) was utilised in the experimental work. The electrical performance of the conductive tip was tested using an AFG2021 signal generator and DMM4050 precision multimeter. The data processing was performed using the SPIP software from Image Metrology [38]. The deterioration of the tip was determined by analysis of the topography measurement data: Ssc (Mean Summit Curvature), which is the average of the principal curvature of the local maximums on the surface, and Sdq6 – the Area Root Mean Square Slope is the root mean square (RMS) value of the surface slope within the sampling area.

An additional parameter – average slope angle (SL), which reveals the angle of the measured slopes of the structures – was introduced. Having in mind that the acquired topography map contains the information about the sample and scanning tip, this data was used to observe the tip deterioration, as the sample was expected to maintain its critical parameters. In order to determine the value, the data was manually extracted and calculated by the profiles analysis of the structure steps. An average value for all X and Y directions was calculated for each set of images, providing a statistical approach. It should be noted that while the appearance of the wear of the test structures was taken into account, the location of the following measurements was constantly changing.

Our experiments were conducted using three samples: i) the assessment of mechanical stability was performed using a structure of a Cr 30 nm layer deposited on a SiO_2 substrate in a magnetron sputtering step; ii) the test of the tip's wear was carried out using a specimen of a Au 80 nm layer deposited on a SiO_2 substrate using thermal evaporation followed by photolithography patterning of the test grid; iii) a HOPG sample was applied to test the electrical performance of the fabricated probes.

3. Results and discussion

3.1. Diamond tip fabrication technology

A commercial microcantilever with a PtIr-coated Si tip (PPP-EFM, Nanosensors) with dimensions: 3 × 225 × 28 μm in thickness, length and width, respectively, and a stiffness of 3.41 N/m was selected for the fabrication of the probe with the SC-BDD tip. A scanning electron microscope micrograph, captured with a current of 0.17nA and an acceleration voltage of 10 kV is shown in Fig. 1a.

The entire fabrication process consists of three steps. After every fabrication step, the thermomechanical noise of the structure was recorded using a laser vibrometer in order to describe the change of the device resonance frequency, thermomechanical vibration amplitude, quality factor, and stiffness. Based on the recorded parameters, the structure mass change was calculated, which described not only the probe properties but also the FIB milling and tip deposition processes as well.

In the first step, the top of the commercial cantilever with tip was milled to the green dashed line depicted in Fig. 1a. The FIB process was performed using an ion beam with 2.5nA and 0.2nA currents at a 30 kV acceleration voltage. The image of the fabricated tipless structure is shown in Fig. 1b. After the FIB milling, the resonance frequency of the structure was increased to 93.7 kHz, thus its mass was reduced by 48.3 ng. Diamond particles were placed on a Si substrate in a vacuum chamber of SEM (Fig. 1c). A particle over 20 μm height, similar to the tip shape, was selected for transfer.

In the second step, SC-BDD was placed at the top of the tipless cantilever. In this procedure, an easy-lift nanomanipulator was used to select, pick up and transfer a SC-BDD particle to the top of the tipless cantilever. The FIBID procedure was applied, as described in the reference [39], to contact the SC-BDD particle with the cantilever. An ion current of 83 pA at 30 kV was used for the Pt(C) deposition process. In this way, the metal concentration in the Pt(C) matrix was increased [40] and a better electrical contact was obtained between the SC-BDD tip and the conductive beam platform in comparison to the FEBID method [31]. Fig. 1d presents the setup in which the SC-BDD diamond particle was placed on the tipless cantilever using the easy-lift nanomanipulator in the vicinity of a GIS nozzle. The deposited crystal on the cantilever was separated from the nanomanipulator with the ion beam milling of 83 pA at a 30 kV acceleration voltage. In order to increase the strength of the interface layer between the tip and the cantilever platform, an additional FEBID layer was deposited with an e-beam of 1.4 pA at a voltage of 2 kV. The deposited and contacted diamond particle is depicted in Fig. 1e. The mass changes were monitored based on the analysis of the thermomechanical vibration noise. The resonance frequency of the presented structure was decreased to 86.32 kHz and according to (3), the entire structure's mass increased by 5.75 ng (Fig. 2, Table 1). In

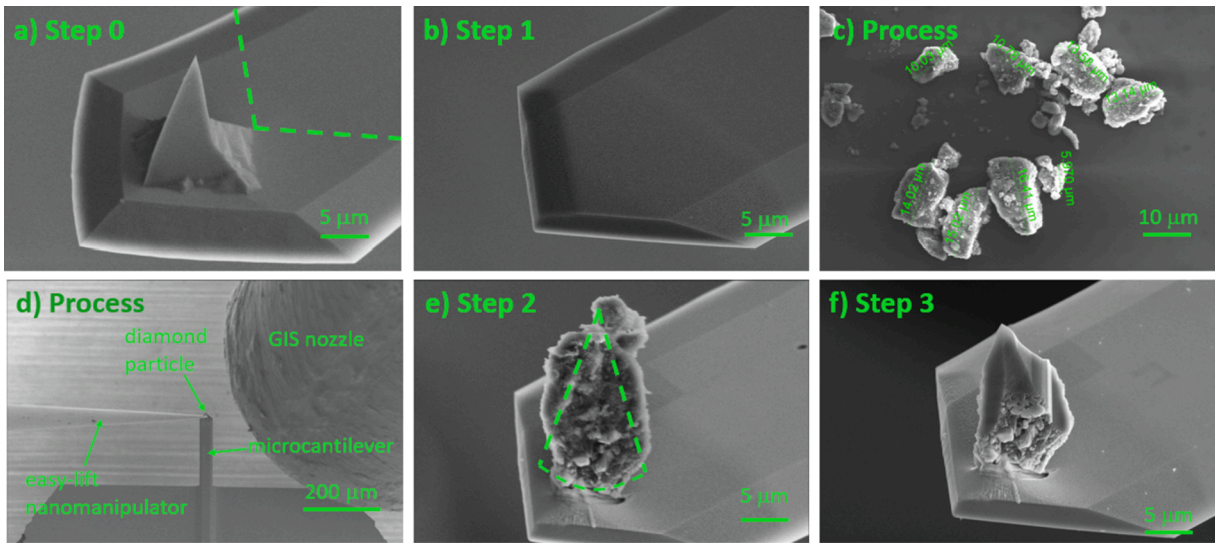

Fig. 1. Fabrication process of the microcantilever with the SC-BDD tip: (a) commercial AFM cantilever with a Si tip as a basic structure (dashed lines indicates the milled area of the cantilever), (b) step 1 – tipless cantilever after FIB milling, (c) BDD particles and clusters with the indicated size on Si wafer surface prepared for the transfer process (e-beam imaging parameters: 0.17nA, 10 kV), (d) the process of diamond particle deposition on the Si cantilever (easy-lift nanomanipulator and GIS nozzle are depicted; e-beam imaging parameters: 0.17 nA, 5 kV), (e) step 2 – BDD particle deposited on the cantilever (dashed lines indicates the cone-shape of tip after FIB milling), (f) step 3 – final FIB milling of the SC-BDD tip (tip radius approximately 70 nm). Imaging parameters for (a), (b), (e), (f) SEM pictures: 10 kV, 0.17 nA; stage tilt angle: 45°; scale bar: 5 µm (Attn. dashed line symbolises the FIB cutting path).

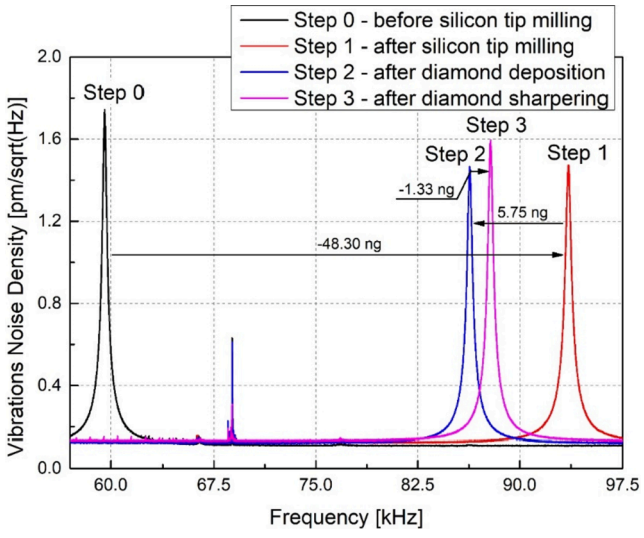

Fig. 2. Thermomechanical noise and mass change determination recorded during fabrication of cantilever equipped with SC-BDD tip.

Table 1
Amplitude of the structure vibration A, resonance frequency f_r, quality factor Q and stiffness k of cantilever according to the thermomechanical characteristics from Fig. 2.

	A [pm/ $\sqrt{Hz}$]	f_r [kHz]	Q	k [N/m]
Step 0 – before silicon tip milling	*1.67*	*59.53*	*217.55*	*3.41*
Step 1 – after silicon tip milling	*1.41*	*93.57*	*251.22*	*3.51*
Step 2 – after diamond deposition	*1.40*	*86.32*	*266.16*	*4.09*
Step 3 – after diamond sharpening	*1.52*	*87.85*	*268.39*	*3.44*

comparison, the mass of the cone-shaped diamond particle (shape indicated by the lines marked in Fig. 1e) was equal to 2.40 ng. This twofold mass drop results from the irregular structure of the particle, whose outer layer is formed by a smaller diamond cluster absorbed electrostatically at the main SC-BDD particle (see Fig. 1e.)

In the third step, the shape of the diamond particle was milled using a Ga ion beam of 83 pA at a 30 kV acceleration voltage to obtain a pyramid-shaped tip (see Fig. 1f). The height of the probe and the tip curvature were approximately 20 µm and 70 nm respectively. The performed FIB milling process could lead to Ga ion implantation and the amorphisation of the particle subsurface [41–42], which could also increase the electrical conductance of the SC-BDD tip. After the final FIB milling, the structure resonance frequency increased to 87.85 kHz which correlated with a mass decrease of 1.33 ng. Therefore, the mass of the SC-BDD particles was estimated as 4.42 ng. The applied mass estimation method is more accurate than geometric calculations due to the irregular shape of the tip, Pt(C) deposition during the mounting process and undesirable Si removal during milling. However, the parameters of the device calculated based on the analysis of the thermomechanical noise are listed in Table 1. The stiffness variations are within 20% tolerance which corresponds with the applied methodology of the stiffness determination [43].

EDS mapping was applied to verify the cantilever composition (see Fig. 3). The analysis indicated the content of carbon (C, Kα = 0.277 eV), silicon (Si, Kα = 1.739 eV) and platinum (Pt, M = 2.048 eV). The shadow effect caused by the EDS detector's location on the upper left side of structure occurs. In these conditions, the boron concentration was below the EDS sensitivity and was not detected. The high carbon content of the tip originates from the SC-BDD. The Si cantilever was also covered with a Pt-containing metal alloy.

Fig. 3b shows a deconvoluted Raman spectrum of the SC-BDD particle measured at room temperature. The Raman spectrum exhibits the characteristic peaks of boron-doped diamond with semi-metallic conductivity [44–45]: a wide band centred around 500 cm^{-1} (referred to as boron-doped band I in this work), a band centred around 1200 cm^{-1} (referred to as boron-doped band II), and the diamond phonon line (1328 cm^{-1}; referred to as the sp^3 peak), which is positioned close to the monocrystalline diamond position (1332.5 cm^{-1}). Boron-doped band I and boron-doped band II appear to be a signature of highly doped

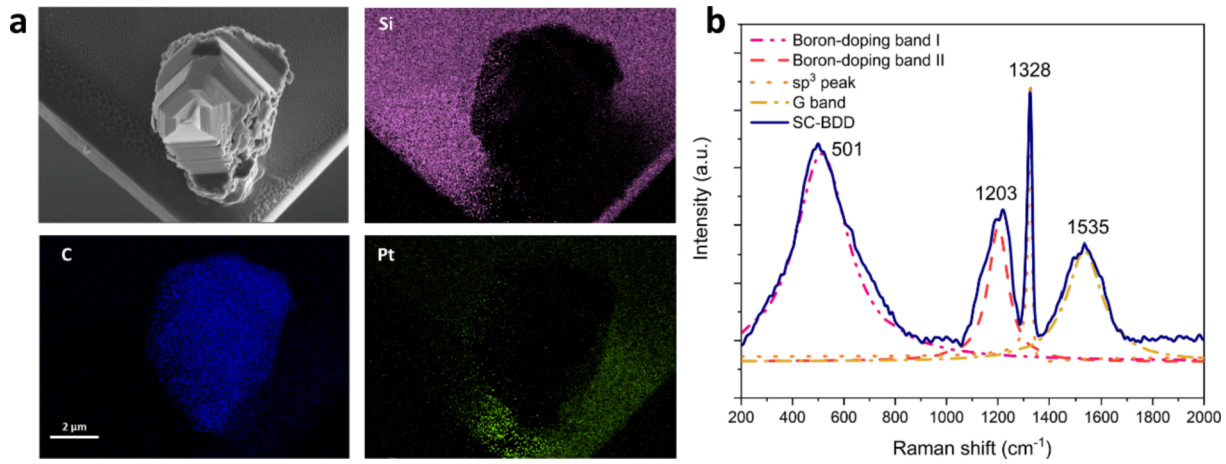

Fig. 3. Probe composition studies: (a) SEM micrograph of analysed area with SC-BDD tip with Si cantilever apex supported by EDS mapping (purple – silicon, blue – carbon, light green – platinum), and (b) deconvoluted Raman spectrum of SC-BDD particle. (For interpretation of the references to colour in this figure legend, the reader is referred to the web version of this article.)

diamond, while their origin is still debatable [46]. The boron and carbon isotopic shifts of the boron-doped band I are not fully consistent in order to assign this line to boron dimers or boron–carbon vibrations [47]. The relationship proposed by Mortet et al. [46] was applied for estimation of boron dopant concentration using Raman spectrum. It is related to the down-shift of the I and II boron-doping Raman band positions. Therefore, the average boron concentration of utilized here boron-doped diamond nanosheets was in the range of 1.0–1.60 10^{21} cm^{-3} [48]. The G band line, characteristic of amorphous carbon, is also evident. A clear and dominant sp^3 peak indicates the highly crystalline nature of the SC-BDD particle. It can be compared to a highly boron-doped monocrystalline diamond synthesised by the HPHT method [49].

3.2. Atomic force microscope measurements

Lateral force microscopy (LFM) measurements were performed using a DI3000 AFM working in ambient conditions. The performed investigations allowed the topography imaging quality to be verified in terms of the tip-cantilever stability, which is essential in terms of the nanoscale measurements. In the performed experiments, the load force setpoint was 80 nN.

In order to observe the quality and repeatability of the friction force measurements, a SiO_2/Cr sample was observed in a series. Sputtered Cr clusters created areas of various friction revealing single grains and interphases between them. In this way, it was possible to observe different areas with a diversity of topography and friction features, which also identified crosstalk between the topography and friction signals. The observation of the grain-friction correlation of the upper and lower part of the image shows that the lateral signal is not influenced by the topography, but it reveals friction phenomena between the SC-BDD tip and the sample surface. It should be noticed that in some cases, grain-to-grain transition reveals a specific lateral force response, whereas in a different spot, a similar feature does not induce the friction response at all. Such an outcome, caused by the diversity of the surface-tip interaction, provides excellent conditions for testing the probe in terms of the normal and lateral force detection stability and selectivity.

As presented in Fig. 4, it is possible to easily distinguish 15 nm features in the area of a 2 × 2 µm scan area, proving satisfying imaging performance in terms of the local resolution. It should be emphasised that as a load force in the range of tens of nN is applied in the measurements, the mechanical impermanence of the probe may appear. This could generate various imaging artifacts related to continuous movement of the scanning tip against the cantilever. While no traces of mechanical instability of the scanning tip were found, the scanning procedure delivered consistent data of nanometre resolution.

Next, the patterned SiO_2/Au surface was applied in order to observe the tip wear. In this case, it was assumed that the steep edges between the Au structure and the SiO_2 substrate should stimulate the tip geometry modifications in the subsequent topography measurements. Therefore, a series of 1550 images with a scan area of 20 × 20 µm (which corresponds to approx. 13.6 m of scanning length) was taken and analysed.

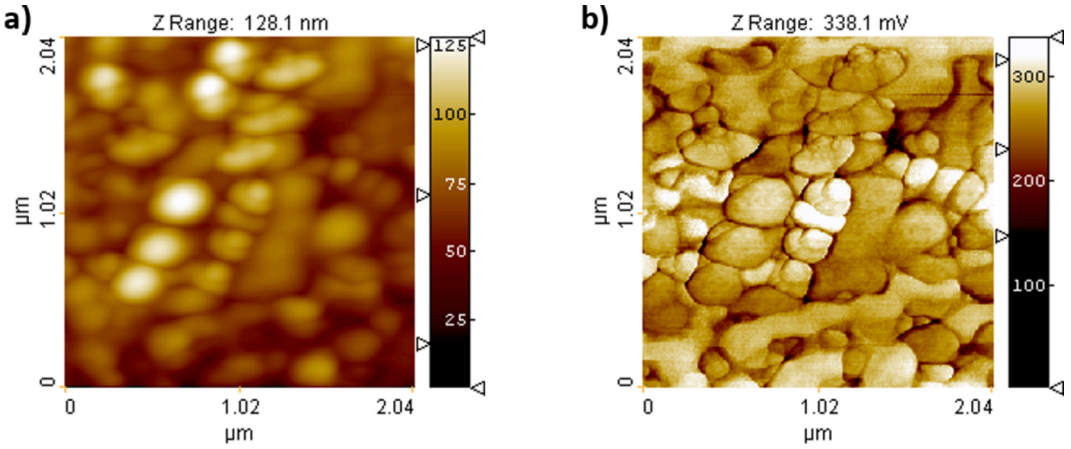

Fig. 4. (a) Topography and (b) friction images recorded on a SiO_2/Cr sample with a cantilever with the SC-BDD tip.

The profiles of the steep edges and the tip geometry were calculated using algorithms available in the SPIP software utilising blind reconstruction methods [50–51]. The result of the calculation performed at the beginning and at the end of the experiments is shown in Fig. 5(a–c). Next to the profile of the reconstructed tip and its 3D visualisation, the topography data used in this procedure is shown. The estimated tip radius was approx. 20 nm, and the cone angle approx. 50°, which meets the demands of the majority of AFM measurements. Control of the tip radius by SEM imaging was abandoned due to possible contamination effects of the probe [52]. Deposition of a thin layer of amorphous carbon would affect the electrical properties of the SC BDD tip and decrease SPM imaging resolution.

It should be emphasised that each measurement was performed in a new sample location in order to avoid the impact of the possible test structure modifications which could occur at a higher load force acting at the tip. The result of the tip reconstruction after 1550 imaging processes, which corresponded with a scanning line with a length of approximately 13.6 m, is shown in Fig. 5(d–f). The estimated average radius of the SC-BDD was 140 nm, and cone angle 140°. It should be stated that due to the relatively small height of the test structures, the cone angle value estimation reflects mostly the tip curvature.

It should be noticed that CVD diamond tips fabricated by Smirnov *et al.* [19] revealed comparable wear behaviour to that presented here in the SC-BDD structures, manifesting minor degradation of imaging resolution after more than 80 scans (length of 30 cm during 18 h of operation). Similarly, Fletcher *et al.* [53] reported no signs of delamination along with 100-fold lower wear rates of approx. 1×10^{-16} m^3 N^{-1} m^{-1} than reported for Si tips. In general, the small wear rate in diamond is attributed to the gradual atom-by-atom attrition at the sliding surface. Nanocrystalline diamond [54] also showed the effect of debris creation induced by the wear process, which consisted of the fractured discrete pieces or amorphised sections. This effect could be a cause of the reduction of the SC-BDD tip radius observed here. SC-BDD particles are predominantly terminated by H and OH groups which were to be removed mechanically from the diamond exposing strong C-C bonds along the interface [55] modifying the friction and wear. This process fluctuates by group re-saturation as a function of the environmental conditions [56] and scanning length, partially explaining the alterations recorded (see Fig. 5 c, f). Interestingly, FIB-fabricated nanoneedles with sub-micro-metre diameters could be reversibly deformed revealing high tensile strains (~9%) [57–59] allowing for high loading and long exposures to the strain as applied in the papers. Buijnsters *et al.* [60] showed that the wear rate increases by a factor of 3 when the B-doping level in the diamond is increased from 0.6 to 2.8 at.%. Since here approximately 2.5% of B dopant was used, the wear resistance of the boron-doped particles would be reduced. The observed initial FIB-milled radius drop could be attributed to both a tip crack at SCD defects or even planarisation of the diamond surface during sliding caused by mechanochemical amorphisation of the diamond. The B-B and B-C bonds, being weaker than C-C, could be broken during a tip run affected by the relatively high level of incorporation of boron. This effect was also supported by *ab-initio* simulations [61] reporting enhanced ductility of diamond induced by substitutional boron doping. Despite the fact of the observed significant change of the tip parameters, one can notice still satisfying surface imaging quality while the very long measurement series was performed. Based on the obtained data, one should emphasise the excellent durability and wear resistance of the fabricated probe. The diamond-based probes are specifically addressed to large scanning areas and have outstanding stability, resolving important issues in tip-based nanofabrication [53].

In order to test the electrical probe parameters, 100 current/voltage (I/V) curves on a HOPG sample were recorded. As shown in Fig. 6, a stable and linear response was obtained. The acquired data revealed time-stable ohmic contact. No indication of tip degradation due to scanning with a large load force was observed so far. However, it is worth to note that the surface of HOPG sample may have been partially chemically etched. The contact resistance of the complete circuit with the probe was determined to be 1450 Ohms. In addition, measurements of the resistance's contribution of particular parts of the developed probe were carried out using precisely positioned electrodes. The chip (bulk part of the probe, providing support for the cantilever, shown partially in the lower part of Fig. 1d) and cantilever were taken into account. The obtained data allowed the resistances of 20 Ohms and 200 Ohms, respectively, to be determined. In this case, the low resistivity of the probe should be attributed to the SC-BDD tip and its proper mounting at the cantilever tip.

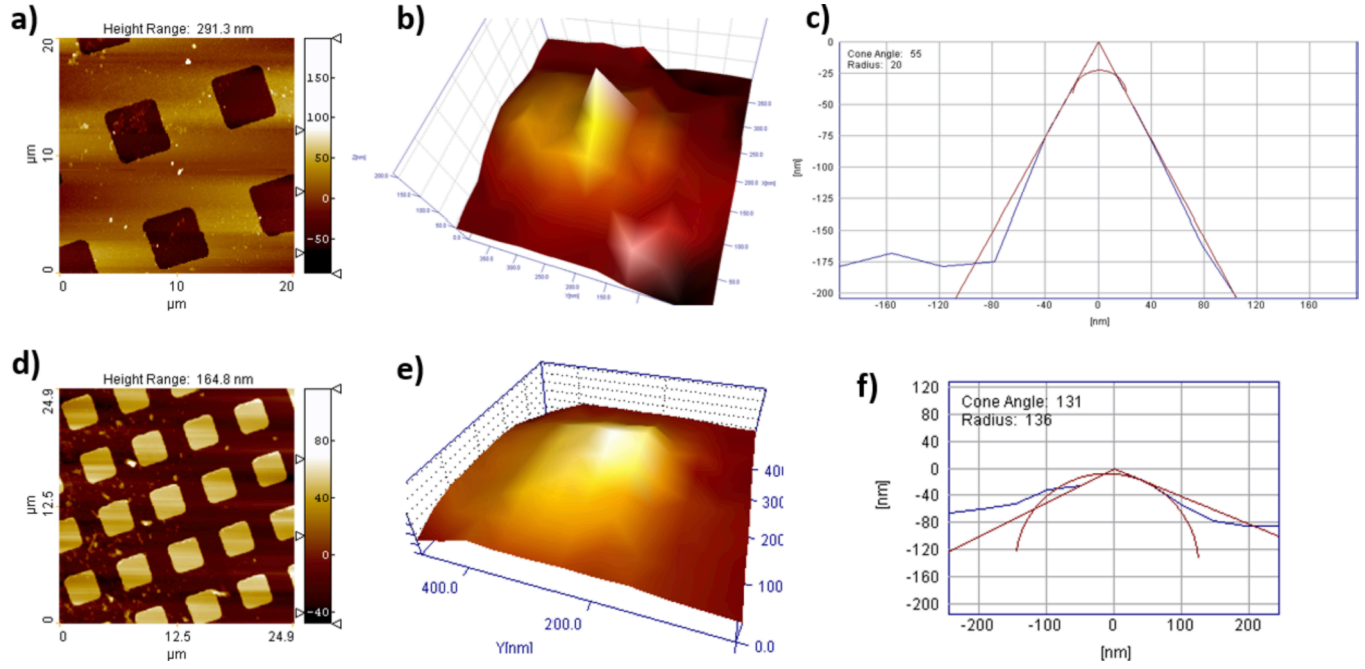

Fig. 5. (a) Topography of patterned SiO_2/Au sample, (b) 3D image of the tip reconstruction, (c) cross-section of reconstructed SC-BDD tip and its parameters performed at the beginning of the experiment, and (d), (e), (f) at the end of the experiment, respectively.

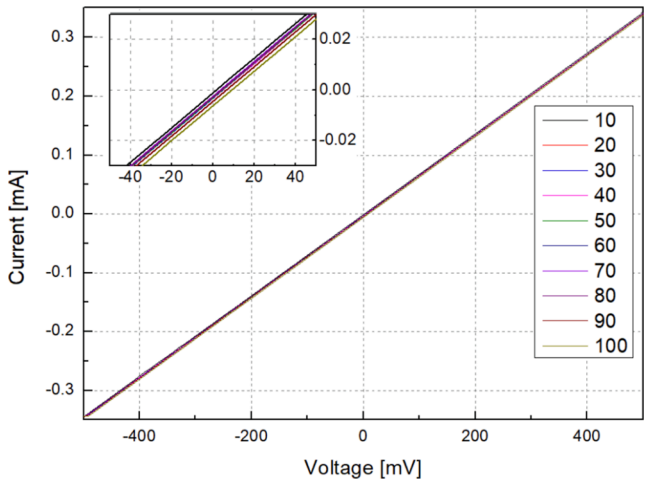

Fig. 6. Series of I/V curves of 100 voltage scans of HOPG sample recorded by cantilever equipped with a SC-BDD tip. (Every line corresponds to the first dataset averaged from the series of ten measurements).

In general, in order to obtain a conductive SCD tip, it is required to implant boron into the bulk HPHT crystal [62] or to apply *in-situ* doping in the CVD process [63]. Nevertheless, implanted solid diamonds are too heavy and blunted, limiting their resolution. Wolf *et al.* [62] reported 6.5 kOhm serial resistances attributed to the diamond tip. HFCVD-grown polycrystalline BDD pyramid tips manifested much lower resistivity values in the order of 10^{-3} Ohm cm as reported by Malave *et al.* [63]. Such an approach also resulted in a radius of 30 nm. Here, the SC-BDD particle tip revealed a serial resistance of 1 kOhm, corresponding to 0.01 Ohm cm [30] since the crystal was isolated from the top surface of delaminated free-standing diamond foil. The corresponding crystal resistivity is one order of magnitude larger than those reported by Malave *et al.* [63], while single-crystal diamond was utilised as a tip limiting the conduction pathways generated by inter-grain sp^2-rich regions. It should be noted that the approach presented here allows the effect of boron incorporation suppression in the early growth phases caused by surface-adsorbed or residual oxygen to be avoided [64]. Oxygen starts to form both stable B-O compounds exhausted from the chamber and to create non-conductive B_xO_y impurities in the diamond structure. Next, Tsigkourakos *et al.* [65] also revealed the important role of an interface seeded and nucleated by undoped nanodiamond particles, where they evidently impact the resistance resulting in an increase of more than one order of magnitude to 1010 Ohm depending on the seeding density [66]. Here, the undesirable result was avoided by isolating the SC-BDD particle from the top surface of the foil [67]. The boron-doped seeds could also be applied, resulting in a resistance in the range of 10^7 Ohm [66].

After the electrical measurements, the wear tests were resumed using a SiO_2/Au sample. In order to evaluate and quantify the obtained results, *Ssc, Sdq6* and *SL* statistical descriptors were calculated. An example profile of the steep edge of the structure is shown in Fig. 7a. After statistical processing of the abovementioned measurements, the summary of the used descriptors as a function of the following measurements were compared to each other in terms of the appearance of specific trends.

The obtained comparison is displayed in Fig. 7b. The graph reveals very stable values of the *Ssc*, *Sdq6* and *SL* parameters during the first 280 measurements. The total scanning length of the SC-BDD tip until the imaging quality drop shown in Fig. 7b was estimated to 0.82 m. It should be underlined that the electrical evaluation was performed in approximately the middle of that stage, when 150 topography measurements showed no deterioration of the imaging quality. The measurements following the electrical evaluation presented no significant deterioration of the tip shape and its imaging quality until the drop point, which was marked on Fig. 7b.

The specific drop of the scanning tip parameters was indicated by all utilised statistical descriptors. The measurement was continued in order to detect any further events in the degradation process. Yet, no additional changes occurred and all parameters showed considerable stability until the measurement number reached 1550. The total travel length of the scanning tip was more than 13.6 m. Concerning the observed single image quality drop event, it was assumed to be caused by a sudden tip deterioration (crack-related damage due to a large load force applied to the probe). Therefore, tip shape reconstruction was performed in order to detect the assumed apex radius increase (see Fig. 5f).

The summarized overview of properties of diamond-based cantilevers are listed in the Table 2. The unique SC-BDD-based probe design is based on high-quality conductive single-crystal diamond particle grown by CVD delivering high in-situ doping concentration material, which is not defected by implantation or contaminated by metal impurities utilized as catalyst during HPHT synthesis. Such a design showed insusceptibility against thermal drift and reliability of the mechanical calibration tuned directly by FIB milling. It also not suffer from polycrystalline multifaceted nature of boron-dopant heterogeneities revealing various electronic behaviour [24]. Finally, the designed SC-BDD tip with Si cantilever revealed the resonance frequency of 86.32 kHz and stiffness of 3.44 N/m, for high-resolution imaging or force modulation measurements, while commercial probes offer much larger spring constants mostly in the range ~ 70–80 N/m and resonance frequency of 200 kHz-400 kHz exhibiting limited sensitivity [70–71].

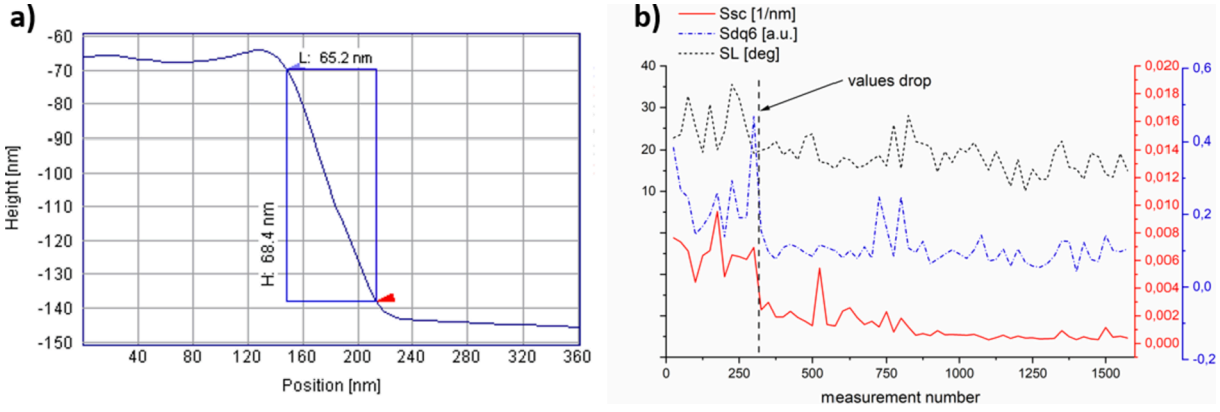

Fig. 7. (a) Example of the test structure's profile used for slope angle determination (*SL* parameter). (b) Surface quality of the surface imaging recorded using a cantilever with the BDD tip described using the statistical surface parameters: *Ssc*, *Sdq6* and *SL*.

Table 2
Overview of electromechanical properties of diamond-based cantilevers.

Fabrication Technology	Diamond performance	Cantilever parameters	Application	Reference
Single-crystal diamond tip	HPHT diamond, graphitized	100 N m^{-1} 90 kHz radius of 30 nm	Field Emission Scanning Probe Lithography	[18]
FIB-sharpened diamond grown at Si tip, tuned by RIE	PA CVD diamond, boron-doped	0.5 N m^{-1} 370 kHz radius of 50 nm	combined AFM-SECM	[19–20]
FIB-sharpened diamond grown at Si tip	PA CVD diamond, in situ boron doped	0.08–6 N m^{-1} 11–110 kHz radius of 20 nm	Conductive Atomic Force Microscopy	[2]
All-diamond tip grown in the etched Si wafer	HF CVD diamond	35.2 N m^{-1} 37.1 kHz radius of 50 nm	Scanning Spreading Resistance Measurements	[26,68]
Boron-implanted diamond plate polished	HPHT diamond	radius of 100 nm	Scanning Tunneling Microscope	[69]
Silicon tip overgrown by diamond,	CVD diamond, nanocrystalline in-situ boron doped, highly conductive,	3.2 N m^{-1} 35.87 kHz radius of 700 nm	Micro- And Nanomechanical Devices	[28]
FIB/FEBID/FIBID of single-crystal BDD particle	CVD diamond, in-situ boron doped, highly conductive,	3.44 N m^{-1} 86.32 kHz radius of 70 nm	Long Distance High Resolution Conductance Imaging	This work

4. Conclusions

SC-BDD particles grown by the microwave plasma enhanced chemical vapour deposition method and mechanically separated from the substrate were used to fabricate microcantilever tips for AFM. The diamond tip fabrication process was performed in the vacuum chamber of a SEM/FIB system. In conclusion, three crucial steps were featured: cantilever preparation for deposition and milling a Si tip with FIB, deposition of SC-BDD particle on the tipless cantilever by FIBID/FEBID technology, formation of the diamond particle into a tip shaped structure with a nanometre curvature radius using FIB. The mass of the diamond tip after the three-step-process was equal to 4.42 ng. The cantilever was tested in LFM-AFM measurements with a load force of approximately 80 nN. Next, 1550 tests of SiO_2/Au topography were performed to verify the wear resistance of the diamond due to strong C-C bonds. Conductivity measurements on a HOPG sample were performed to indicate the contact resistance of 1450 Ohms of SC-BDD. After the tests, a curvature radius decrease was observed from 20 nm to 140 nm.

Future experiments will involve diamond probe interaction with FIB and quantitative research of dopants and/or defects in diamond. Due to the wear resistance properties of diamond tip, further applications could be extended to nanoscratching and nanolithography. A similar SEM/FIB method of fabrication might be applied to deposit a microcantilever tip of a different material.

CRediT authorship contribution statement

Ewelina Gacka: Investigation, Formal analysis, Methodology, Visualization, Writing – original draft, Writing – review & editing. **Piotr Kunicki:** Conceptualization, Methodology, Supervision, Writing – review & editing, Investigation, Formal analysis. **Andrzej Sikora:** Investigation, Methodology, Visualization, Writing – original draft, Writing – review & editing. **Robert Bogdanowicz:** Resources, Supervision, Writing – review & editing, Funding acquisition. **Mateusz Ficek:** Investigation, Resources, Visualization, Writing – original draft. **Teodor Gotszalk:** Conceptualization, Project administration, Writing – review & editing, Funding acquisition. **Ivo W. Rangelow:** Supervision, Writing – review & editing. **Krzysztof Kwoka:** Writing – review & editing, Investigation.

Declaration of Competing Interest

The authors declare that they have no known competing financial interests or personal relationships that could have appeared to influence the work reported in this paper.

References

[1] S. Koizumi, C. Nebel, M. Nesladek, eds., Physics and Applications of CVD Diamond, Wiley (2008). https://doi.org/10.1002/9783527623174.
[2] A. Olbrich, B. Ebersberger, C. Boit, P. Niedermann, W. Hänni, J. Vancea, H. Hoffmann, High aspect ratio all diamond tips formed by focused ion beam for conducting atomic force microscopy, J. Vac. Sci. Technol. B Microelectron. Nanom. Struct. 17 (1999) 1570, https://doi.org/10.1116/1.590842.
[3] I.W. Rangelow, F. Shi, P. Hudek, P. Grabiec, B. Volland, E.I. Givargizov, A. N. Stepanova, L.N. Obolenskaya, E.S. Mashkova, V.A. Molchanov, Micromachined ultrasharp silicon and diamond-coated silicon tip as a stable field-emission electron source and a scanning probe microscopy sensor with atomic sharpness, J. Vac. Sci. Technol. B Microelectron. Nanom. Struct. 16 (1998) 3185, https://doi.org/10.1116/1.590348.
[4] A.N. Stepanova, Preparation of ultrasharp diamond tip emitters by ion-beam etching, J. Vac. Sci. Technol. B Microelectron. Nanom. Struct. 16 (1998) 678, https://doi.org/10.1116/1.589879.
[5] K. Hirama, H. Takayanagi, S. Yamauchi, J.H. Yang, H. Kawarada, H. Umezawa, Spontaneous polarization model for surface orientation dependence of diamond hole accumulation layer and its transistor performance, Appl. Phys. Lett. 92 (2008), 112107, https://doi.org/10.1063/1.2889947.
[6] W. Gajewski, P. Achatz, O.A. Williams, K. Haenen, E. Bustarret, M. Stutzmann, J. A. Garrido, Electronic and optical properties of boron-doped nanocrystalline diamond films, Phys. Rev. B. 79 (2009), 045206, https://doi.org/10.1103/PhysRevB.79.045206.
[7] J. Bousquet, T. Klein, M. Solana, L. Saminadayar, C. Marcenat, E. Bustarret, Phase diagram of boron-doped diamond revisited by thickness-dependent transport studies, Phys. Rev. B. 95 (2017), 161301, https://doi.org/10.1103/PhysRevB.95.161301.
[8] J. Liu, T. Teraji, B. Da, Y. Koide, High Output Current Boron-Doped Diamond Metal-Semiconductor Field-Effect Transistors, IEEE Electron Device Lett. 40 (2019) 1748–1751, https://doi.org/10.1109/LED.2019.2942967.
[9] S. Baluchová, A. Daňhel, H. Dejmková, V. Ostatná, M. Fojta, K. Schwarzová-Pecková, Recent progress in the applications of boron doped diamond electrodes in electroanalysis of organic compounds and biomolecules – A review, Anal. Chim. Acta. 1077 (2019) 30–66, https://doi.org/10.1016/j.aca.2019.05.041.
[10] S.J. Cobb, Z.J. Ayres, J.V. Macpherson, Boron Doped Diamond: A Designer Electrode Material for the Twenty-First Century, Annu. Rev. Anal. Chem. 11 (2018) 463–484, https://doi.org/10.1146/annurev-anchem-061417-010107.
[11] T. Zhao, X. Wang, F. Sun, The effects of boron doping on residual stress of hfcvd diamond film for mems applications, Surf. Rev. Lett. 25 (2018) 1850039, https://doi.org/10.1142/S0218625X18500397.
[12] M. Vojs, M. Marton, M. Jančo, M. Behúl, V. Řeháček, P. Michniak, M. Držík, R. Redhammer, Fabrication of boron doped diamond cantilevers by means of dry ICP etching, J. Phys. Conf. Ser. 1319 (2019), 012015, https://doi.org/10.1088/1742-6596/1319/1/012015.
[13] O. Shenderova, N. Nunn, Production and purification of nanodiamonds, in: Nanodiamonds, Elsevier (2017) 25–56. https://doi.org/10.1016/B978-0-32-343029-6.00002-7.
[14] S. Heyer, W. Janssen, S. Turner, Y.-G. Lu, W.S. Yeap, J. Verbeeck, K. Haenen, A. Krueger, Toward Deep Blue Nano Hope Diamonds: Heavily Boron-Doped Diamond Nanoparticles, ACS Nano. 8 (2014) 5757–5764, https://doi.org/10.1021/nn500573x.
[15] T. Kondo, Electrochemical Applications of Conductive Diamond Powders, in: Yang N. (eds) Novel Aspects of Diamond. Topics in Applied Physics, Springer, Cham. 121 (2019) 477–496. https://doi.org/10.1007/978-3-030-12469-4_14.
[16] E.I. Givargizov, A.N. Stepanova, L.L. Aksenova, E.V. Rakova, J.L. Hatchison, N. A. Kiselev, E.S. Mashkova, V.A. Molchanov, Nucleation and growth of crystalline diamond particles on silicon tips, Crystallogr. Reports. 47 (2002) S159–S168, https://doi.org/10.1134/1.1529970.
[17] T. Hantschel, T. Conard, J. Kilpatrick, G. Cross, Diamond Probes Technology, in: Celano U. (eds) Electrical Atomic Force Microscopy for Nanoelectronics. NanoScience and Technology. Springer, Cham. (2019) 351–384. https://doi.org/10.1007/978-3-030-15612-1_11.
[18] M. Hofmann, C. Lenk, T. Ivanov, I.W. Rangelow, A. Reum, A. Ahmad, M. Holz, E. Manske, Field emission from diamond nanotips for scanning probe lithography, J. Vac. Sci. Technol. B. 36 (2018) 06JL02, https://doi.org/10.1116/1.5048193.

[19] W. Smirnov, A. Kriele, R. Hoffmann, E. Sillero, J. Hees, O.A. Williams, N. Yang, C. Kranz, C.E. Nebel, Diamond-Modified AFM Probes: From Diamond Nanowires to Atomic Force Microscopy-Integrated Boron-Doped Diamond Electrodes, Anal. Chem. 83 (2011) 4936–4941, https://doi.org/10.1021/ac200659e.
[20] A. Eifert, W. Smirnov, S. Frittmann, C. Nebel, B. Mizaikoff, C. Kranz, Atomic force microscopy probes with integrated boron doped diamond electrodes: Fabrication and application, Electrochem. Commun. 25 (2012) 30–34, https://doi.org/10.1016/j.elecom.2012.09.011.
[21] D.P. Adams, M.J. Vasile, T.M. Mayer, V.C. Hodges, Focused ion beam milling of diamond: Effects of H2O on yield, surface morphology and microstructure, J. Vac. Sci. Technol. B Microelectron. Nanom. Struct. 21 (2003) 2334, https://doi.org/10.1116/1.1619421.
[22] A. Eifert, P. Langenwalter, J. Higl, M. Lindén, C.E. Nebel, B. Mizaikoff, C. Kranz, Focused ion beam (FIB)-induced changes in the electrochemical behavior of boron-doped diamond (BDD) electrodes, Electrochim. Acta. 130 (2014) 418–425, https://doi.org/10.1016/j.electacta.2014.03.029.
[23] J. Hu, K.B. Holt, J.S. Foord, Focused Ion Beam Fabrication of Boron-Doped Diamond Ultramicroelectrodes, Anal. Chem. 81 (2009) 5663–5670, https://doi.org/10.1021/ac9003908.
[24] J. Ryl, L. Burczyk, A. Zielinski, M. Ficek, A. Franczak, R. Bogdanowicz, K. Darowicki, Heterogeneous oxidation of highly boron-doped diamond electrodes and its influence on the surface distribution of electrochemical activity, Electrochim. Acta. 297 (2019) 1018–1027, https://doi.org/10.1016/j.electacta.2018.12.050.
[25] K. Arstila, T. Hantschel, C. Demeulemeester, A. Moussa, W. Vandervorst, Microfabricated diamond tip for nanoprobing, Microelectron. Eng. 86 (2009) 1222–1225, https://doi.org/10.1016/j.mee.2008.11.061.
[26] E. Oesterschulze, A. Malavé, U.F. Keyser, M. Paesler, R.J. Haug, Diamond cantilever with integrated tip for nanomachining, Diam. Relat. Mater. 11 (2002) 667–671, https://doi.org/10.1016/S0925-9635(01)00542-8.
[27] A.N. Obraztsov, P.G. Kopylov, B.A. Loginov, M.A. Dolganov, R.R. Ismagilov, N. V. Savenko, Single crystal diamond tips for scanning probe microscopy, Rev. Sci. Instrum. 81 (2010), 013703, https://doi.org/10.1063/1.3280182.
[28] R. Bogdanowicz, M. Sobaszek, M. Ficek, D. Kopiec, M. Moczała, K. Orłowska, M. Sawczak, T. Gotszalk, Fabrication and characterization of boron-doped nanocrystalline diamond-coated MEMS probes, Appl. Phys. A. 122 (2016) 270, https://doi.org/10.1007/s00339-016-9829-9.
[29] R. Bogdanowicz, M. Ficek, M. Sobaszek, A. Nosek, Ł. Gołuński, J. Karczewski, A. Jaramillo-Botero, W.A. Goddard, M. Bockrath, T. Ossowski, Growth and Isolation of Large Area Boron-Doped Nanocrystalline Diamond Sheets: A Route toward Diamond-on-Graphene Heterojunction, Adv. Funct. Mater. 29 (2019) 1805242, https://doi.org/10.1002/adfm.201805242.
[30] M. Rycewicz, M. Ficek, K. Gajewski, S. Kunuku, J. Karczewski, T. Gotszalk, I. Wlasny, A. Wysmołek, R. Bogdanowicz, Low-strain sensor based on the flexible boron-doped diamond-polymer structures, Carbon N. Y. 173 (2021) 832–841, https://doi.org/10.1016/j.carbon.2020.11.071.
[31] I. Utke, P. Hoffmann, J. Melngailis, Gas-assisted focused electron beam and ion beam processing and fabrication, J. Vac. Sci. Technol. B Microelectron. Nanom. Struct. 26 (2008) 1197, https://doi.org/10.1116/1.2955728.
[32] J.L. Hutter, J. Bechhoefer, Calibration of atomic-force microscope tips, Rev. Sci. Instrum. 64 (1993) 1868–1873, https://doi.org/10.1063/1.1143970.
[33] H.-J. Butt, M. Jaschke, Calculation of thermal noise in atomic force microscopy, Nanotechnology. 6 (1995) 1–7, https://doi.org/10.1088/0957-4484/6/1/001.
[34] D. Dontsov, E. Langlotz, Interferometer characterizes microstructures. On the track of the nanometer [Online]. Available: https://sios-de.com/wp-content/uploads/2015/09/NA-NMM_engl.pdf. (Accessed: 14 April 2021).
[35] J. te Riet, A.J. Katan, C. Rankl, S.W. Stahl, A.M. van Buul, I.Y. Phang, A. Gomez-Casado, P. Schön, J.W. Gerritsen, A. Cambi, A.E. Rowan, G.J. Vancso, P. Jonkheijm, J. Huskens, T.H. Oosterkamp, H. Gaub, P. Hinterdorfer, C.G. Figdor, S. Speller, Interlaboratory round robin on cantilever calibration for AFM force spectroscopy, Ultramicroscopy. 111 (2011) 1659–1669, https://doi.org/10.1016/j.ultramic.2011.09.012.
[36] G. Jóźwiak, D. Kopiec, P. Zawierucha, T. Gotszalk, P. Janus, P. Grabiec, I. W. Rangelow, The spring constant calibration of the piezoresistive cantilever based biosensor, Sensors Actuators B Chem. 170 (2012) 201–206, https://doi.org/10.1016/j.snb.2012.02.007.
[37] K. Kwoka, K. Orłowska, W. Majstrzyk, A. Sierakowski, P. Janus, D. Tomaszewski, P. Grabiec, T. Piasecki, T. Gotszalk, Soft piezoresistive cantilevers for adhesion force measurements, Sensors Actuators A Phys. 301 (2020), 111747, https://doi.org/10.1016/j.sna.2019.111747.
[38] SPIP Classic Roughness Parameters for Images [Online]. Available: http://www.imagemet.com/WebHelp6/Default.htm#RoughnessParameters/Roughness_Parameters.htm#Mean_Summit_Curvature_Ssc. (Accessed: 10 April 2021).
[39] B. Świadkowski, W. Majstrzyk, P. Kunicki, A. Sierakowski, T. Gotszalk, Near-zero contact force atomic force microscopy investigations using active electromagnetic cantilevers, Nanotechnology. 31 (2020), 425706, https://doi.org/10.1088/1361-6528/aba0f2.
[40] J.M. De Teresa, R. Córdoba, A. Fernández-Pacheco, O. Montero, P. Strichovanec, M.R. Ibarra, Origin of the Difference in the Resistivity of As-Grown Focused-Ion- and Focused-Electron-Beam-Induced Pt Nanodeposits, J. Nanomater. 2009 (2009) 1–11, https://doi.org/10.1155/2009/936863.
[41] S. Rubanov, A. Suvorova, Ion implantation in diamond using 30keV Ga+ focused ion beam, Diam. Relat. Mater. 20 (2011) 1160–1164, https://doi.org/10.1016/j.diamond.2011.06.027.
[42] S. Rubanov, A. Suvorova, V.P. Popov, A.A. Kalinin, Y.N. Pal'yanov, Fabrication of graphitic layers in diamond using FIB implantation and high pressure high temperature annealing, Diam. Relat. Mater. 63 (2016) 143–147, https://doi.org/10.1016/j.diamond.2015.11.017.
[43] N.A. Burnham, X. Chen, C.S. Hodges, G.A. Matei, E.J. Thoreson, C.J. Roberts, M. C. Davies, S.J.B. Tendler, Comparison of calibration methods for atomic-force microscopy cantilevers, Nanotechnology. 14 (2003) 1–6, https://doi.org/10.1088/0957-4484/14/1/301.
[44] P.W. May, W.J. Ludlow, M. Hannaway, P.J. Heard, J.A. Smith, K.N. Rosser, Raman and conductivity studies of boron-doped microcrystalline diamond, facetted nanocrystalline diamond and cauliflower diamond films, Diam. Relat. Mater. 17 (2008) 105–117, https://doi.org/10.1016/j.diamond.2007.11.005.
[45] M. Bernard, C. Baron, A. Deneuville, About the origin of the low wave number structures of the Raman spectra of heavily boron doped diamond films, Diam. Relat. Mater. 13 (2004) 896–899, https://doi.org/10.1016/j.diamond.2003.11.082.
[46] V. Mortet, Z. Vlčková Živcová, A. Taylor, O. Frank, P. Hubík, D. Trémouilles, F. Jomard, J. Barjon, L. Kavan, Insight into boron-doped diamond Raman spectra characteristic features, Carbon N. Y. 115 (2017) 279–284, https://doi.org/10.1016/j.carbon.2017.01.022.
[47] V.A. Sidorov, E.A. Ekimov, Superconductivity in diamond, Diam. Relat. Mater. 19 (2010) 351–357, https://doi.org/10.1016/j.diamond.2009.12.002.
[48] R. Bogdanowicz, M. Ficek, N. Malinowska, S. Gupta, R. Meek, P. Niedziałkowski, M. Rycewicz, M. Sawczak, J. Ryl, T. Ossowski, Electrochemical performance of thin free-standing boron-doped diamond nanosheet electrodes, J. Electroanal. Chem. 862 (2020), https://doi.org/10.1016/j.jelechem.2020.114016.
[49] N. Dubrovinskaia, L. Dubrovinsky, N. Miyajima, F. Langenhorst, W.A. Crichton, H. F. Braun, High-pressure / High-temperature Synthesis and Characterization of Boron-doped Diamond, Zeitschrift Für Naturforsch. B. 61 (2006) 1561–1565, https://doi.org/10.1515/znb-2006-1213.
[50] J.S. Villarrubia, Algorithms for scanned probe microscope image simulation, surface reconstruction, and tip estimation, J. Res. Natl. Inst. Stand. Technol. 102 (1997) 425, https://doi.org/10.6028/jres.102.030.
[51] P.M. Williams, Blind reconstruction of scanning probe image data, J. Vac. Sci. Technol. B Microelectron. Nanom. Struct. 14 (1996) 1557, https://doi.org/10.1116/1.589138.
[52] A. Vladar, M. Postek, Electron Beam-Induced Sample Contamination in the SEM, Microsc. Microanal. 11 (2005), https://doi.org/10.1017/S1431927605507785.
[53] P.C. Fletcher, J.R. Felts, Z. Dai, T.D. Jacobs, H. Zeng, W. Lee, P.E. Sheehan, J. A. Carlisle, R.W. Carpick, W.P. King, Wear-Resistant Diamond Nanoprobe Tips with Integrated Silicon Heater for Tip-Based Nanomanufacturing, ACS Nano. 4 (2010) 3338–3344, https://doi.org/10.1021/nn100203d.
[54] R.A. Bernal, R.W. Carpick, Visualization of nanoscale wear mechanisms in ultrananocrystalline diamond by in-situ TEM tribometry, Carbon N. Y. 154 (2019) 132–139, https://doi.org/10.1016/j.carbon.2019.07.082.
[55] J. Liu, D.S. Grierson, N. Moldovan, J. Notbohm, S. Li, P. Jaroenapibal, S. D. O'Connor, A.V. Sumant, N. Neelakantan, J.A. Carlisle, K.T. Turner, R. W. Carpick, Preventing Nanoscale Wear of Atomic Force Microscopy Tips Through the Use of Monolithic Ultrananocrystalline Diamond Probes, Small. 6 (2010) 1140–1149, https://doi.org/10.1002/smll.200901673.
[56] A.R. Konicek, D.S. Grierson, P.U.P.A. Gilbert, W.G. Sawyer, A.V. Sumant, R. W. Carpick, Origin of Ultralow Friction and Wear in Ultrananocrystalline Diamond, Phys. Rev. Lett. 100 (2008), 235502, https://doi.org/10.1103/PhysRevLett.100.235502.
[57] A. Nie, Y. Bu, P. Li, Y. Zhang, T. Jin, J. Liu, Z. Su, Y. Wang, J. He, Z. Liu, H. Wang, Y. Tian, W. Yang, Approaching diamond's theoretical elasticity and strength limits, Nat. Commun. 10 (2019) 5533, https://doi.org/10.1038/s41467-019-13378-w.
[58] A. Banerjee, D. Bernoulli, H. Zhang, M.-F. Yuen, J. Liu, J. Dong, F. Ding, J. Lu, M. Dao, W. Zhang, Y. Lu, S. Suresh, Ultralarge elastic deformation of nanoscale diamond, Science 360 (2018) 300–302, https://doi.org/10.1126/science.aar4165.
[59] B. Regan, A. Aghajamali, J. Froech, T.T. Tran, J. Scott, J. Bishop, I. Suarez-Martinez, Y. Liu, J.M. Cairney, N.A. Marks, M. Toth, I. Aharonovich, Plastic Deformation of Single-Crystal Diamond Nanopillars, Adv. Mater. 32 (2020) 1906458, https://doi.org/10.1002/adma.201906458.
[60] J.G. Buijnsters, M. Tsigkourakos, T. Hantschel, F.O.V. Gomes, T. Nuytten, P. Favia, H. Bender, K. Arstila, J.-P. Celis, W. Vandervorst, Effect of Boron Doping on the Wear Behavior of the Growth and Nucleation Surfaces of Micro- and Nanocrystalline Diamond Films, ACS Appl. Mater. Interfaces. 8 (2016) 26381–26391, https://doi.org/10.1021/acsami.6b08083.
[61] B. Yang, X. Peng, C. Huang, Y. Zhao, X. Chen, G. Zhang, T. Fu, Toughening and maintaining strength of diamond with substitutional doping boron and nitrogen, J. Alloys Compd. 805 (2019) 1090–1095, https://doi.org/10.1016/j.jallcom.2019.07.090.
[62] P. De Wolf, J. Snauwaert, T. Clarysse, W. Vandervorst, L. Hellemans, Characterization of a point-contact on silicon using force microscopy-supported resistance measurements, Appl. Phys. Lett. 66 (1995) 1530–1532, https://doi.org/10.1063/1.113636.

[63] A. Malavé, E. Oesterschulze, W. Kulisch, T. Trenkler, T. Hantschel, W. Vandervorst, Diamond tips and cantilevers for the characterization of semiconductor devices, Diam. Relat. Mater. 8 (1999) 283–287, https://doi.org/10.1016/S0925-9635(98)00388-4.
[64] M. Tsigkourakos, T. Hantschel, Z. Xu, B. Douhard, J. Meersschaut, Y. Zou, K. Larsson, M. Boman, W. Vandervorst, Suppression of boron incorporation at the early growth phases of boron-doped diamond thin films, Phys. Status Solidi. 212 (2015) 2595–2599, https://doi.org/10.1002/pssa.201532185.
[65] M. Tsigkourakos, T. Hantschel, D.K. Simon, T. Nuytten, A.S. Verhulst, B. Douhard, W. Vandervorst, On the local conductivity of individual diamond seeds and their impact on the interfacial resistance of boron-doped diamond films, Carbon N. Y. 79 (2014) 103–112, https://doi.org/10.1016/j.carbon.2014.07.048.
[66] Z. Xu, T. Hantschel, M. Tsigkourakos, W. Vandervorst, Scanning spreading resistance microscopy for electrical characterization of diamond interfacial layers, Phys. Status Solidi. 212 (2015) 2578–2582, https://doi.org/10.1002/pssa.201532234.
[67] M. Rycewicz, Ł. Macewicz, J. Kratochvil, A. Stanisławska, M. Ficek, M. Sawczak, V. Stranak, M. Szkodo, R. Bogdanowicz, Physicochemical and Mechanical Performance of Freestanding Boron-Doped Diamond Nanosheets Coated with C:H:N: O Plasma Polymer, Materials (Basel). 13 (2020) 1861, https://doi.org/10.3390/ma13081861.
[68] A. Malavé, E. Oesterschulze, All-diamond cantilever probes for scanning probe microscopy applications realized by a proximity lithography process, Rev. Sci. Instrum. 77 (2006), https://doi.org/10.1063/1.2194478.
[69] R. Kaneko, S. Oguchi, Ion-Implanted Diamond Tip for a Scanning Tunneling Microscope, Jpn. J. Appl. Phys. 29 (1990), https://doi.org/10.1143/JJAP.29.1854.
[70] Conductive Diamond Coated AFM Tips [Online]. Available: https://www.nanoandmore.com/conductive-diamond-coated-afm-tips. (Accessed: 16 September 2021).
[71] C. Kranz, Diamond as Advanced Material for Scanning Probe Microscopy Tips, Electroanalysis 28 (2016), https://doi.org/10.1002/elan.201500630.